FEBS 20387 FEBS Letters 430 (1998) 105–111

Minireview

Mapping flexible protein domains at subnanometer resolution with the atomic force microscope

Daniel J. Müller, Dimitrios Fotiadis, Andreas Engel*

M.E. Müller-Institute for Microscopy, Biozentrum, University of Basel, Klingelbergstrasse 70, CH-4056 Basel, Switzerland

Received 16 May 1998

Abstract The mapping of flexible protein domains with the atomic force microscope is reviewed. Examples discussed are the bacteriorhodopsin from *Halobacterium salinarum*, the head-tail-connector from phage ϕ29, and the hexagonally packed intermediate layer from *Deinococcus radiodurans* which all were recorded in physiological buffer solution. All three proteins undergo reversible structural changes that are reflected in standard deviation maps calculated from aligned topographs of individual protein complexes. Depending on the lateral resolution (up to 0.8 nm) flexible surface regions can ultimately be correlated with individual polypeptide loops. In addition, multivariate statistical classification revealed the major conformations of the protein surface.

Key words: Atomic force microscopy; Hexagonally packed intermediate layer; Phage ϕ29 head-to-tail connector; Protein flexibility; Purple membrane

1. Introduction

The function of biomolecules is intimately linked to their three-dimensional structure as well as to their conformational flexibility. While the former is analyzed in most cases by X-ray crystallography, the latter can be assessed by nuclear magnetic resonance provided that the macromolecule has a mass $< 50\,000$ Da. For larger complexes such as membrane proteins embedded in a lipid bilayer or regular protein arrays, the atomic force microscope (AFM [1]) provides a powerful alternative to visualize protein surface fluctuations. The possibility of imaging individual molecules at submolecular resolution under physiological conditions allows the macromolecules to be observed during their work cycle [2]. Although only the surface topography is accessible to the stylus, and the time resolution is limited by the mechanical properties of the cantilever [3], a wealth of information on function related protein conformations can be acquired [4].

As discussed in this review, the comparison of a large set of images from identical molecules recorded in different conformations reveals structure-function relationships. While crystallographic analyses with either electron or X-ray beams require proteins to be locked in a single conformation, the much superior signal-to-noise (S/N) ratio of surface contour measurements with the AFM [5–8] allows a mixture of conformations to be studied. In fact, as demonstrated here, a quantitative analysis of proteins subjected to conditions that promote conformational transitions may be advantageous.

To this end, individual molecular topographs must be aligned translationally and angularly with respect to a suitable reference [9]. This step requires some fixed features of the surface structure in spite of conformational flexibility. In addition, the selection of the reference is critical as it may have a profound influence on the final result [10]. From sets of aligned molecules standard deviation (SD) maps are calculated to reveal the flexible parts of the protein, while multivariate statistical classifications [11,12] unveil the principal modes of the protein motions.

2. Examples

2.1. The cytoplasmic surface of purple membrane

Purple membranes are part of the inner membrane of *Halobacterium salinarum*, and consist of bacteriorhodopsin and lipids all packed into a two-dimensional crystal [13]. These highly ordered 2D trigonal lattices ($a = b = 6.2$ nm) have allowed the seven transmembrane α-helices of bacteriorhodopsin to be resolved [14]. Some of the α-helices undergo conformational changes during light-driven proton translocation [15,16]. The three-dimensional atomic structure of bacteriorhodopsin has been solved by electron crystallography [17,18] and X-ray crystallography [19]. Interestingly, all three atomic models provided different surface structures. Apparently, the preparation methods for electron microscopy or the 3D crystallization had an influence on the flexible surface structures. The most native environment to maintain the surface structure of purple membrane is an aqueous electrolyte solution [20]. Thus, the AFM operated in physiological buffer solutions was expected to provide additional information. Indeed, force-induced reversible conformational changes of individual helix-connecting loops have been observed with the AFM, indicating where the most flexible loops of the cytoplasmic bacteriorhodopsin surface are located [7].

At forces of 100 pN applied to the tip (in the following referred as applied force), the cytoplasmic surface revealed bacteriorhodopsin trimers with three peripheral protrusions of 0.6 ± 0.1 nm height (Fig. 1a,b). These protrusions correlate with the long loops connecting transmembrane α-helices E and F [7]. Fig. 1c displays the SD map which shows pronounced maxima located at the positions of the topographic protrusions (Fig. 1b). Three-fold symmetrization enhanced the structure of the bacteriorhodopsin trimer (average in Fig. 1d)

*Corresponding author. Fax: (41) (61) 267 2109.
E-mail: aengel@ubaclu.unibas.ch

Abbreviations: AFM, atomic force microscopy; HPI layer, hexagonally packed intermediate layer; RMS, root-mean-square; SD, standard deviation; S/N, signal-to-noise

PII: S0014-5793(98)00623-1

as well as the SD map (Fig. 1e). As indicated with contours in Fig. 1d, maxima (0.25 nm) of the symmetrized standard deviation map (Fig. 1e) coincided laterally within ±0.2 nm with the topographic protrusions. Height fluctuations were smaller over the lipid moiety as indicated by a standard deviation of 0.1 nm.

When the applied force was ≥300 pN, the pronounced protrusions at the periphery of trimers vanished and the cytoplasmic surface of bacteriorhodopsin trimers converted into a donut-shaped structure of height 0.4 ± 0.1 nm (Fig. 2a). At such forces the tip pushed the prominent E-F loop of each bacteriorhodopsin monomer away [7]. Occasionally individual monomers were missing as can be seen due to the high S/N ratio of the topograph. The monomer now had two distinct protrusions close to the center of the trimer, while the third protrusion only occasionally appeared at the periphery of the trimer. Although the correlation average of the trimer showed all three protrusions of bacteriorhodopsin monomers (Fig. 2b), the peripheral protrusion was less distinct after averaging than in the unprocessed data (Fig. 2a). After three-fold symmetrization, the outer protrusions vanished while the two inner protrusions of the monomer became more distinct (Fig. 2d). In contrast, the SD map revealed three maxima per trimer (Fig. 2c) that correlated with the position of the E-F loops, as indicated by contours in Fig. 2b. After three-fold symmetrization the SD map exhibited peripheral maxima of 0.19 nm at the position of the E-F loops, while the standard deviation over the lipid was 0.08 nm (Fig. 2e).

To further analyze the conformations of the E-F loop, the unit cells of a topograph recorded at applied forces varying linearly from 100 pN to 300 pN during the scan (data not shown, [7]) were extracted, aligned with respect to a reference, and classified by principal component analysis [11,12]. The three-fold symmetrized averages of the major classes shown in Fig. 2f–i reveal the movement of the flexible loops. The classes were closely related to the force gradient: whereas the force of the averaged topograph shown in Fig. 2f was close to 300 pN, the force in Fig. 2g was 200 pN. Decreasing the force to 150 pN resulted in a rather drastic conformational change of the E-F loop (Fig. 2h). At 100 pN the E-F loop protruded fully out of the surface (Fig. 2i; compare with Fig. 1d).

2.2. The phage φ29 head-tail connector

The head and tail of complex bacteriophages are joined by a connector that plays a role in head assembly as well as DNA packaging and translocation [21]. Head-tail connectors have been studied by electron microscopy and found to possess a narrow cylindrical end that interacts with the tail, and a wide cylindrical end that interfaces with the head. By 3D reconstruction a central channel has been observed [22] that is probably required for translocating the DNA [23]. Connectors exhibit 12-fold [8,24] as well as 13-fold rotational symmetry [25,26]. This interesting polymorphism fostered different models for the DNA packaging mechanism. Necks of bacteriophage φ29 that consist of the connector protein

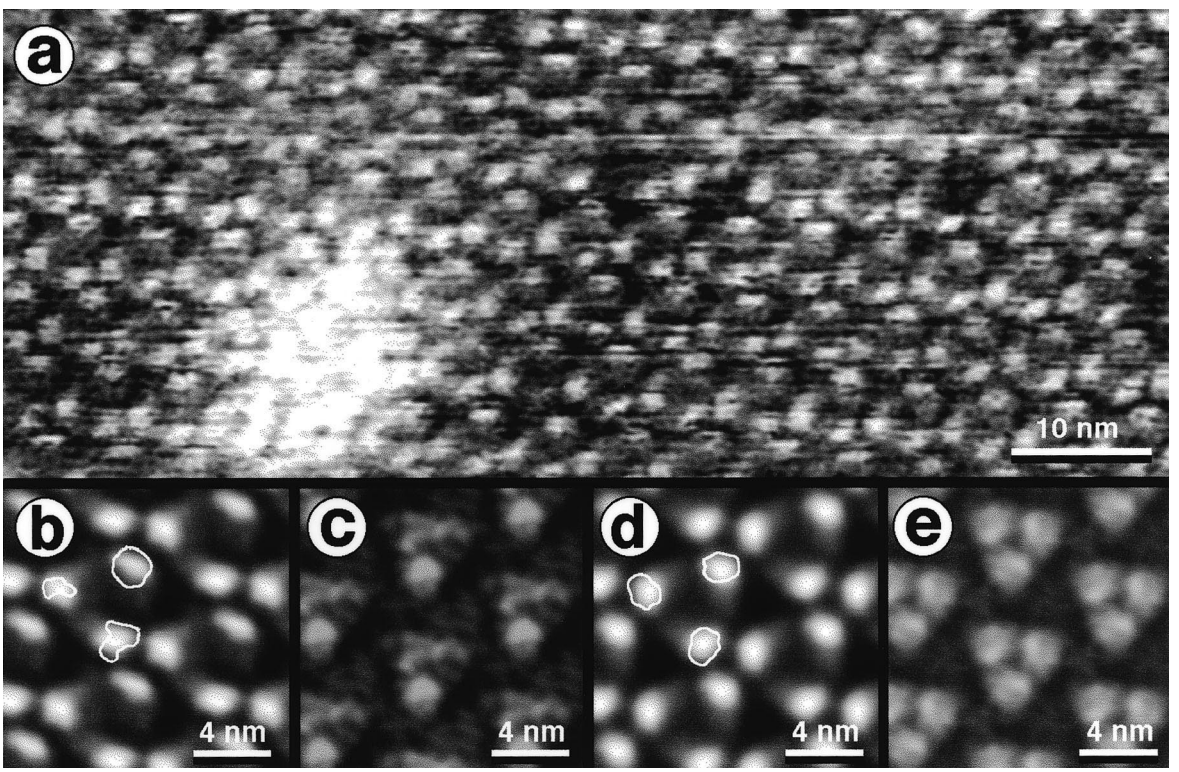

Fig. 1. AFM topograph of the cytoplasmic purple membrane surface recorded at an applied force of 100 pN. a: Raw data obtained in 150 mM KCl, pH 9.2, 10 mM Tris-HCl. b: Correlation average of a ($n = 420$). c: Standard deviation (SD) map of the correlation average. d: Three-fold symmetrized correlation average (9.5% RMS deviation from three-fold symmetry). e: three-fold symmetrized SD map. In both averaged topographs contours of their SD map are outlined. Full gray level ranges: 1.5 nm (a), 1 nm (b and d). Minima and maxima of the SD maps were 0.12 nm and 0.29 nm for c, and 0.10 nm and 0.25 nm for e. Sample preparation and imaging conditions were as described [35,38]. The SEMPER image processing system was used to calculate correlation averages [36]. SD maps were generated according to Schabert and Engel [32].

and an additional subunit exhibit a 12-folded rotational symmetry, and represent the native DNA packing protein. ϕ29 connectors can be crystallized into highly ordered 2D crystals that have been studied by cryo-electron microscopy to a resolution of 0.9 nm [24].

Fig. 3a displays ϕ29 connectors crystallized into a square lattice of dimensions $a = b = 16.5 \pm 0.5$ nm. Unit cells consist of two connectors oriented in opposite directions, consistent with the space group $p42_12$ [24]. The narrow end protruded by 2.3 ± 0.2 nm above the rosette of the thicker connector end. The flexibility of the narrow end limited the resolution and led to instabilities along the fast scan direction [8]. When the applied force was increased from 50 pN to 100–150 pN the narrow connector end was bent away undergoing a reversible, force-dependent conformational change [8]. The wider connector end showed 12 subunits exhibiting a right-handed vorticity. Occasionally individual or multiple subunits of the connector ends were missing (Fig. 3a).

After correlation averaging details of the wider connector end became more distinct (Fig. 3b), whereas the narrow end remained blurred. Accordingly, the SD map exhibited a maximum (0.42 nm) at the periphery of the narrow connector end (Fig. 3c). After four-fold symmetrization the 12 subunits of the wide connector end had a corrugation of 0.3 ± 0.1 nm, while the connector channel had a diameter of 3.5 ± 0.3 nm (Fig. 3d). The narrow end had an outer diameter of 6.4 ± 0.4 nm and a channel whose inner diameter was 3.7 ± 0.3 nm. The four-folded SD map exhibited minima (0.2 nm) over the protrusions of the wider connector end, reflecting the relative stiffness of this structure. Larger height fluctuations occurred between the rosettes of the wide connector end resulting in a standard deviation of 0.28 nm. The largest fluctuations were

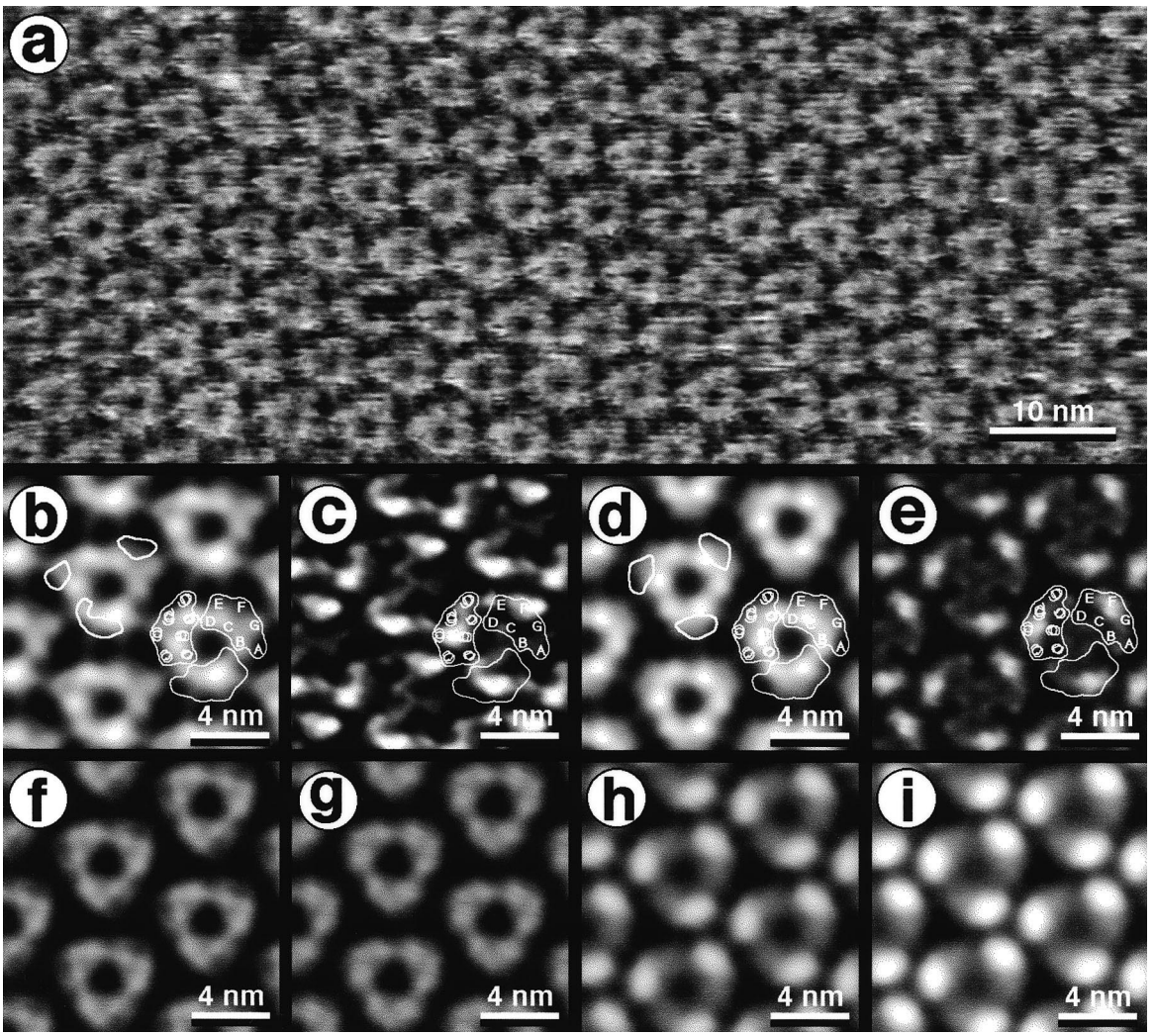

Fig. 2. AFM topograph of the cytoplasmic purple membrane surface recorded at an applied force of 300 pN. a: Raw data obtained in 150 mM KCl, pH 9.2, 10 mM Tris-HCl. b: Correlation average of a ($n = 451$). c: SD map of the correlation average. d: Three-fold symmetrized correlation average (13.3% RMS deviation). e: Three-fold symmetrized SD map. In both averaged topographs contours of their SD map and of the projection map revealed by electron crystallography [17] are outlined. f–i: Three-fold symmetrized averaged topographs calculated from unit cells classified by multivariate statistical analysis [12]. Unit cells were classified by an algorithm kindly provided by J.-P. Bretaudiere [37]. f: Purple membrane imaged at a slightly reduced force compared to d ($n = 105$; 19.2% RMS deviation). g: Same membrane imaged at an applied force of approximately 200 pN ($n = 48$; 16.9% RMS deviation). h: Membrane imaged at approximately 150 pN ($n = 73$; 14.1% RMS deviation). i: Purple membrane imaged at an applied force of approximately 100 pN ($n = 218$; 9.0% RMS deviation; see Fig. 1d). Full gray level ranges: 1 nm (a), 0.5 nm (b and d), and 0.8 nm (f–i). Minima and maxima of the SD maps were 0.08 nm and 0.23 nm for c, and 0.08 nm and 0.19 nm for e.

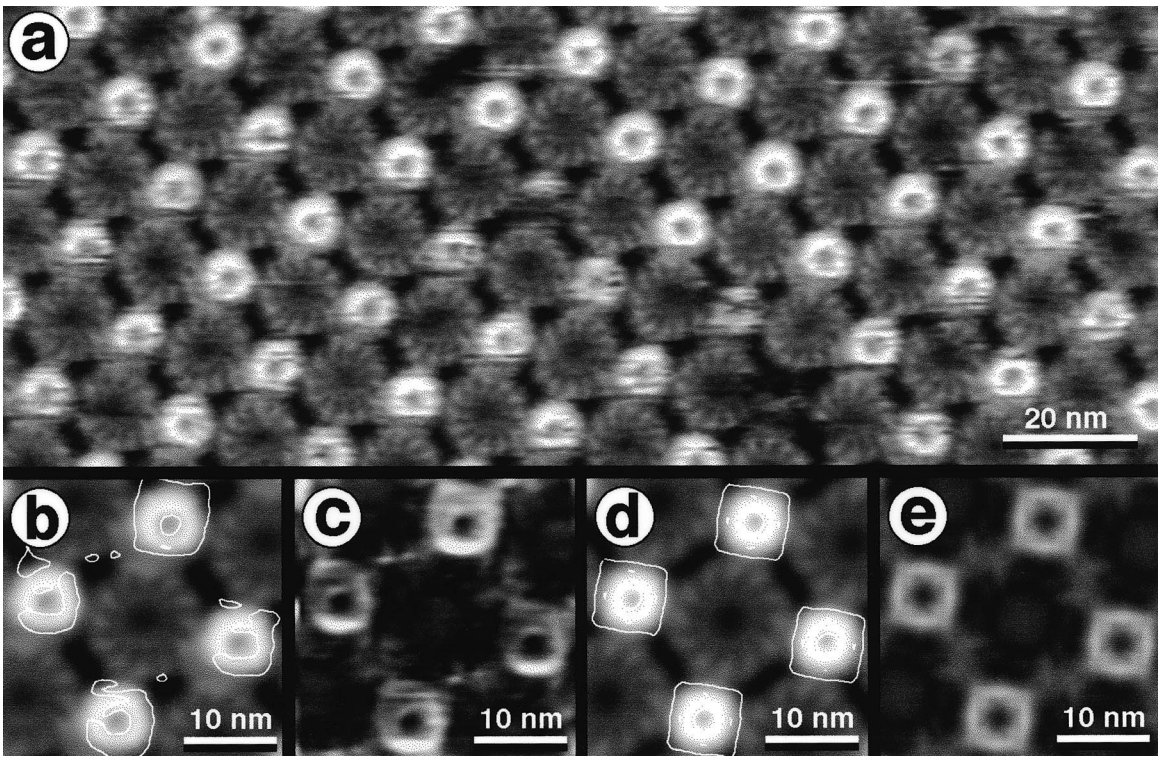

Fig. 3. AFM topograph of the head-to-tail connector of the bacteriophage ϕ29. a: Raw data obtained in 500 mM KCl, pH 7.8, 10 mM Tris-HCl. b: Correlation average of a ($n = 307$). c: SD map of the correlation average. d: Four-fold symmetrized correlation average (8.9% RMS deviation). e: Four-fold symmetrized SD map. In both averaged topographs contours of their SD map are outlined. Full gray level ranges: 4 nm (a), and 3 nm (b and d). Minima and maxima of the SD maps were 0.18 nm and 0.73 nm for c, and 0.11 nm and 0.51 nm for e. Sample preparation and imaging conditions were as described [8,38].

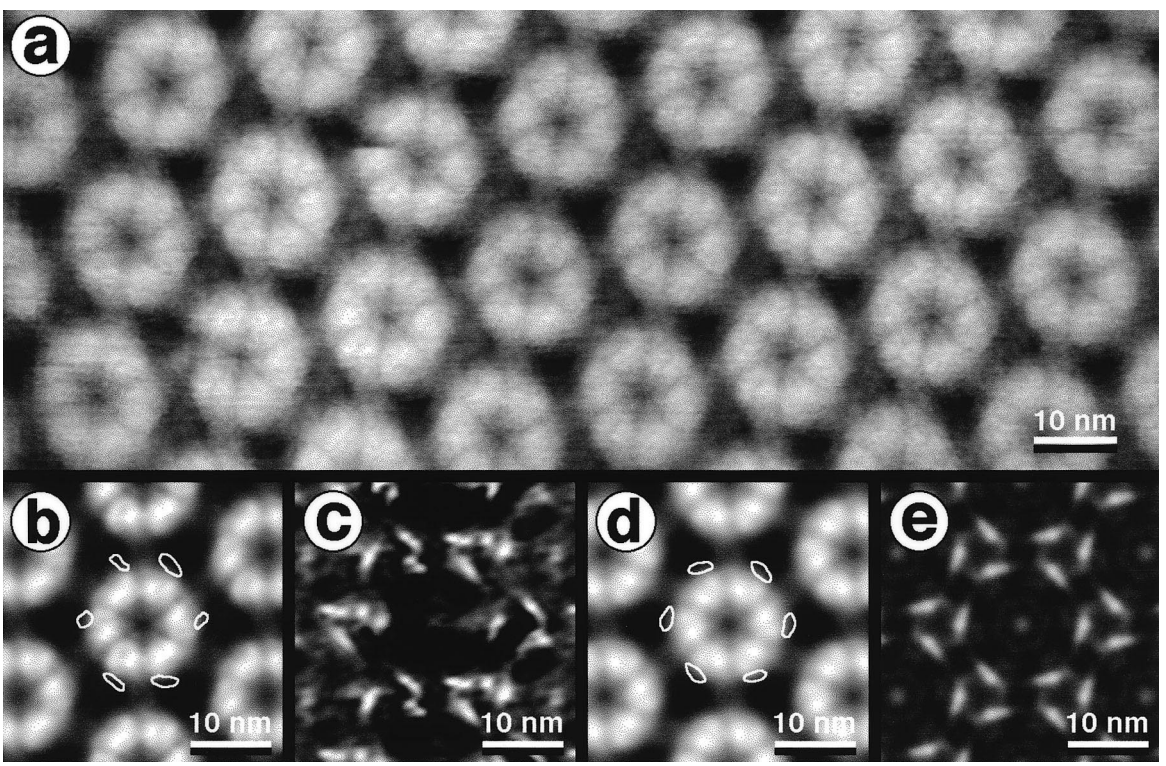

Fig. 4. AFM topograph of the outer surface of the HPI layer. a: Raw data obtained in 150 mM KCl, pH 7.8, 10 mM Tris-HCl. b: Correlation average of a ($n = 79$). c: SD map of the correlation average. d: Six-fold symmetrized correlation average (2.8% RMS deviation). e: Six-fold symmetrized SD map. In both averaged topographs contours of their SD map are outlined. Full gray level ranges: 4 nm (a), and 3 nm (b and d). Minima and maxima of the SD maps were 0.07 nm and 0.80 nm for c, and 0.11 nm and 0.34 nm for e. Sample preparation and imaging conditions were as described [29,38].

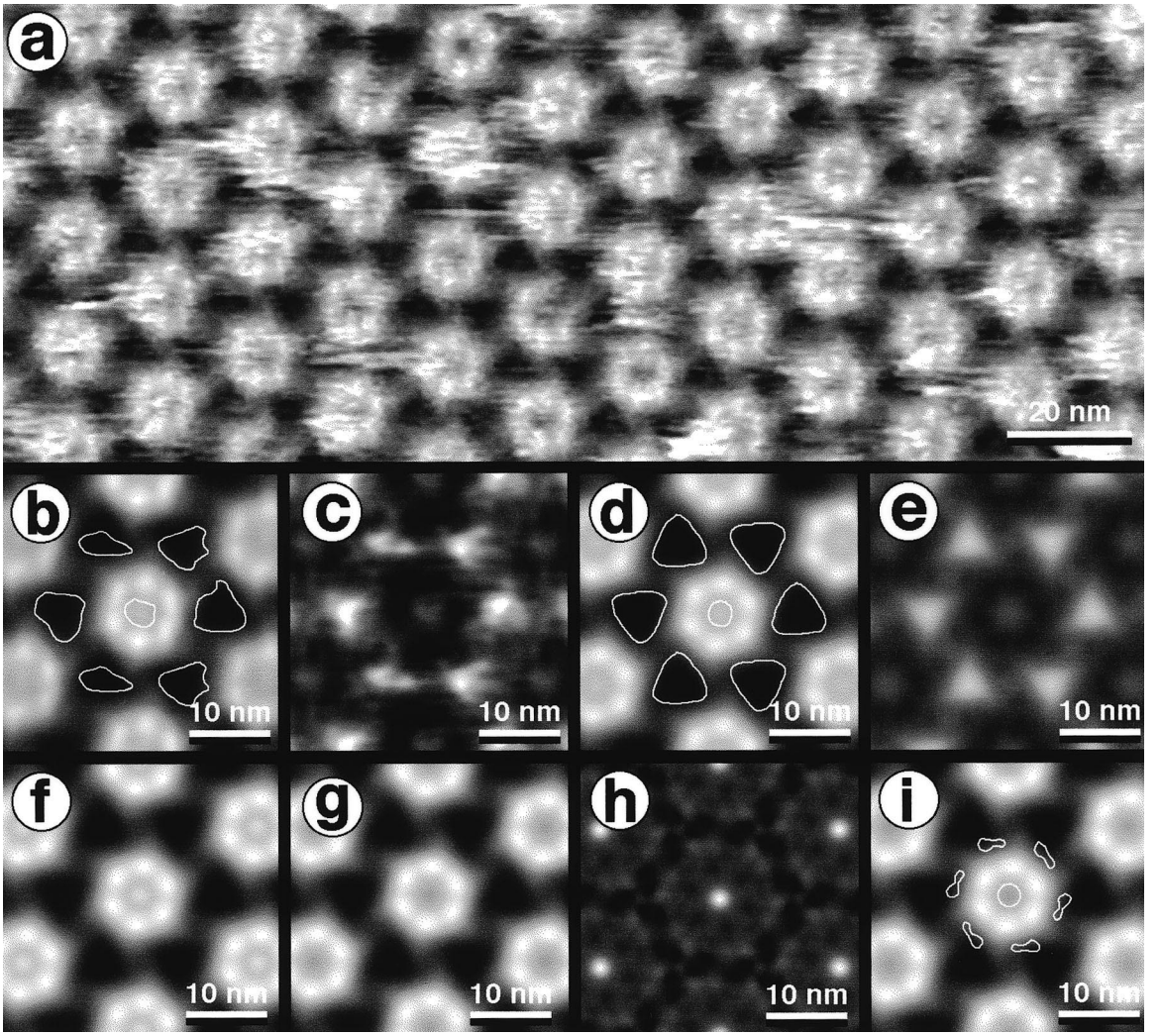

Fig. 5. AFM topograph of the inner surface of the HPI layer. a: Raw data obtained in 150 mM KCl, pH 7.8, 10 mM Tris-HCl. b: Correlation average of a ($n = 332$). c: SD map of the correlation average. d: Six-fold symmetrized correlation average (0.8% RMS deviation). e: Six-fold symmetrized SD map. In both averaged topographs contours of their SD map are outlined. Averaged and six-fold symmetrized topographs of the open (f; $n = 25$; 1.0% RMS deviation) and closed (g; $n = 54$; 1.0% RMS deviation) conformation calculated from unit cells classified by multivariate statistical analysis. h: Difference map between f and g. i: Open conformation with the contours of the difference map (h). The contours of the surroundings were drawn at half maximum. Full gray level ranges: 4 nm (a), 3 nm (b, d, f, g, and i), and 0.8 nm (h). Minima and maxima of the SD maps were 0.25 nm and 1.01 nm for c, and 0.38 nm and 0.86 nm for e.

found at the rim of the narrow connector ends (0.51 nm), but when the tip penetrated into the channel, the structure apparently stiffened as revealed by a standard deviation of 0.11 nm over the channel (Fig. 3e).

2.3. The HPI layer

The hexagonally packed intermediate (HPI) layer, a typical bacterial surface layer, is the major cell envelope protein of the radiotolerant bacterium *Deinococcus radiodurans* [27]. The HPI layer has been characterized biochemically [27], by electron microscopy [28] and by atomic force microscopy [5,29]. Assembled from one protein (M_r 107 028 Da; [30]) that forms hexamers of M_r 655 000 Da [31], the HPI layer is a hexagonal lattice with a unit cell size of 18 nm. According to the 3D model from electron microscopy [28] one hexagonal unit is comprised of a massive core from which six thin spokes emanate to connect adjacent units.

As revealed by the AFM the outer surface of the HPI layer consists of donut-shaped hexamers, featuring six V-shaped protrusions and spokes that form the intermolecular links (Fig. 4a). Correlation averages show these features more clearly (Fig. 4b). The SD map had maxima (0.8 nm) between adjacent HPI cores (Fig. 4c). Six-fold symmetrization further enhanced the V-shaped protrusions and the spokes (Fig. 4d), while the symmetrized SD map (Fig. 4e) showed maxima (0.34 nm) in the open areas between the spokes.

The inner surface of the HPI layer exhibited two conformations (Fig. 5a). Again, each core was assembled from six morphological units, but an additional mass sometimes appeared to plug the central pore. This conformation was time-dependent, and individual pores were observed to reversibly switch from one state to the other within a few minutes [29]. If such 'open' and 'closed' HPI cores are correlation-averaged, the signal of the plugs was reduced while the six subunits of the core and the spokes were enhanced (Fig. 5b). The SD map had six maxima (1.01 nm) located between the spokes, and a weak but distinct maximum that was located about the six-fold axis (0.63 nm; Fig. 5c). Six-fold symmetrization im-

proved the features of the protein (Fig. 5d), as well as those of the SD map (Fig. 5e).

Particle classification by principal component analysis depends on the features addressed. Using the inter-core variations to classify the particles yielded class averages that were not interpretable, whereas classification with respect to the plug region showed two classes, the 'closed' (Fig. 5f) and the 'open' (Fig. 5g) states. The difference map from both conformations showed the central plug and indicated that the rim of the plugged pore was slightly enlarged (Fig. 5h). To relate these differences to the HPI structure, the outline of the difference map was superimposed on the open conformation (Fig. 5i).

3. Discussion and conclusions

Although the high S/N ratio of AFM topographs is sufficient to resolve individual proteins and their subunits, correlation averaging further enhances common structural details [32]. An excellent correlation between averaged AFM topographs and 3D structures obtained by other techniques was observed in case of the outer surface of the HPI layer [5] and of porin OmpF [6]. In addition, by aligning topographs of identical protein complexes, SD maps could be calculated which reflected flexible protein regions rather than the noise of the imaging process [5,32]. In this review we expand these findings by processing topographs of different protein arrays and by using multivariate statistical analysis to classify individual proteins according to their conformation. As demonstrated with bacteriorhodopsin, certain structural features can be partly or entirely lost in the averaged topograph whereas they are distinct in SD maps. The prominent cytoplasmic loop connecting transmembrane α-helices E and F was imaged at low forces in the extended conformation (Fig. 1) yielding the most significant protrusion of the bacteriorhodopsin surface. However, this prominent loop was pushed away by the interaction with the AFM tip at high forces [7], revealing the shorter loops connecting transmembrane α-helices A-B and C-D. In the SD map, however, the E-F loops were distinct (Fig. 2e).

A similar effect was observed on the narrow end of the ϕ29 phage head-tail connector. This end is the most flexible part of the connector [8] and is thought to undergo conformational changes during the translocation of DNA [23]. Although the narrow ends were imaged in their extended conformation at forces of 50–100 pN (Fig. 3a) their flexibility prevented high-resolution imaging. The SD map exhibited maxima at the periphery of the narrow ends, whereas the 12 protrusions of the wide end exhibited a standard deviation which was about 2.5 times lower. The central region of the wide connector end had an intermediate standard deviation (Fig. 3e). The flexibility of this channel region is probably important for the DNA translocation. Most amazing, however, is the low standard deviation at the channel center of the narrow connector end, suggesting a stiffening of this structure by the interaction with the tip.

A rather high standard deviation was measured when the AFM tip descended between adjacent ϕ29 connectors (Fig. 3e) and between the spokes of the HPI layer cores (Figs. 4e and 5e). Such areas cannot be correlated to the protein structure directly. During imaging the feedback loop of the AFM maintains the force applied to the biological sample constant. Thus, over holes the tip is pushed forward until its side interacts with the rim of the hole. In this case, the contact area between tip and sample is ill defined, thereby explaining the pronounced standard deviation maxima at the periphery of gaps between protein complexes (Fig. 3e, Figs. 4e and 5e).

A low standard deviation (Fig. 4e) was measured on the outer surface of the HPI core with its six V-shaped protrusions (Fig. 4d). The related stiffness of the protein correlates well with the unusual stability of this S layer [27,33,34]. The inner surface of the HPI layer exposed a hexameric core that had a smaller diameter than the outer surface, but a more pronounced central channel which often was found to be closed by a plug (Fig. 5a). Multivariate statistical classification [11,12] was sufficiently sensitive to detect the 'open' and 'closed' states of the channel (Fig. 5f,g).

We show that the standard deviation of the sample height measured for many independent protein units provides quantitative information on the structural flexibility. SD maps exhibit the same lateral resolution as the respective topographs. Thus, flexibility maps with a resolution of better than 1 nm can be recorded, as demonstrated for the cytosolic surface of bacteriorhodopsin. The agreement between the temperature factor of loops established by an extensive electron crystallographic analysis [17] and the SD map from topographs recorded with the AFM substantiates the validity of the latter approach. More important, however, is the possibility to classify the essential surface conformations of identical protein complexes. As demonstrated with bacteriorhodopsin it might be advantageous to observe the protein under conditions that favor the presence of different conformations, thereby promoting the possibility of capturing the full spectrum of states. In this way AFM can be used to follow the motion of protein surfaces at subnanometer resolution.

References

[1] Binnig, G., Quate, C.F. and Gerber, C. (1986) Phys. Rev. Lett. 56, 930–933.
[2] Radmacher, M., Fritz, M., Hansma, H.G. and Hansma, P.K. (1994) Science 265, 1577–1579.
[3] Butt, H.-J., Siedle, P., Seifert, K., Fendler, K., Seeger, T., Bamberg, E., Weisenhorn, A.L., Goldie, K. and Engel, A. (1993) J. Microsc. 169, 75–84.
[4] Müller, D.J., Schoenenberger, C.-A., Schabert, F. and Engel, A. (1997) J. Struct. Biol. 119, 149–157.
[5] Karrasch, S., Hegerl, R., Hoh, J., Baumeister, W. and Engel, A. (1994) Proc. Natl. Acad. Sci. USA 91, 836–838.
[6] Schabert, F.A., Henn, C. and Engel, A. (1995) Science 268, 92–94.
[7] Müller, D.J., Büldt, G. and Engel, A. (1995) J. Mol. Biol. 249, 239–243.
[8] Müller, D.J., Engel, A., Carrascosa, J. and Veléz, M. (1997) EMBO J. 16, 101–107.
[9] Frank, J. and Boublik, M. (1981) Science 214, 1353–1355.
[10] Penczek, P., Radermacher, M. and Frank, J. (1992) Ultramicroscopy 40, 33–53.
[11] van Heel, M. (1984) Ultramicroscopy 13, 165–184.
[12] Frank, J., Bretaudiere, J.-P., Carazo, J.-M., Veschoor, A. and Wagenknecht, T. (1987) J. Microsc. 150, 99–115.
[13] Kates, M., Kushawa, S.C. and Sprott, G.D. (1982) Methods Enzymol. 88, 98–111.
[14] Henderson, R., Baldwin, J.M., Ceska, T.A., Zemlin, F., Beckman, E. and Downing, K.H. (1990) J. Mol. Biol. 213, 899–929.
[15] Dencher, N.A., Dresselhaus, D., Zaccai, G. and Büldt, G. (1989) Proc. Natl. Acad. Sci. USA 86, 7876–7879.
[16] Subramaniam, S., Gerstein, M., Oesterhelt, D. and Henderson, R. (1993) EMBO J. 12, 1–8.

[17] Grigorieff, N., Ceska, T.A., Downing, K.H., Baldwin, J.M. and Henderson, R. (1996) J. Mol. Biol. 259, 393–421.
[18] Kimura, Y., Vassylev, D.G., Miyazawa, A., Kidera, A., Matsushima, M., Mitsuoka, K., Murata, K., Hirai, T. and Fujiyoshi, Y. (1997) Nature 389, 206–211.
[19] Pebay-Peyroula, E., Rummel, G., Rosenbusch, J.P. and Landau, E.M. (1997) Science 277, 1676–1681.
[20] Sass, H.J., Schachowa, I.W., Rapp, G., Koch, M.H.J., Oesterhelt, D., Dencher, N.A. and Büldt, G. (1997) EMBO J. 16, 1484–1491.
[21] Valpuesta, J.M. and Carrascosa, J.L. (1994) Q. Rev. Biophys. 27, 107–155.
[22] Carazo, J.M., Santisteban, A. and Carrascosa, J.L. (1985) J. Mol. Biol. 183, 79–88.
[23] Carrascosa, J.L., Carazo, J.M., Herranz, L., Donate, L.E. and Secilla, J.P. (1990) Computers Math. Applic. 20, 57–65.
[24] Valpuesta, J.M., Carrascosa, J.L. and Henderson, R. (1994) J. Mol. Biol. 240, 281–287.
[25] Dube, P., Tavares, P., Lurz, R. and van Heel, M. (1993) EMBO J. 12, 1303–1309.
[26] Tsuprun, V., Anderson, D. and Egelman, E.H. (1994) Biophys. J. 66, 2139–2150.
[27] Baumeister, W., Karrenberg, F., Rachel, R., Engel, A., Ten Heggeler, B. and Saxton, W.O. (1982) Eur. J. Biochem. 125, 535–544.
[28] Baumeister, W., Barth, M., Hegerl, R., Guckenberger, R., Hahn, M. and Saxton, W.O. (1986) J. Mol. Biol. 187, 241–253.
[29] Müller, D.J., Baumeister, W. and Engel, A. (1996) J. Bacteriol. 178, 3025–3030.
[30] Peters, J., Peters, M., Lottspeich, F., Schäfer, W. and Baumeister, W. (1987) J. Bacteriol. 169, 5216–5223.
[31] Engel, A., Baumeister, W. and Saxton, W. (1982) Proc. Natl. Acad. Sci. USA 79, 4050–4054.
[32] Schabert, F.A. and Engel, A. (1994) Biophys. J. 67, 2394–2403.
[33] Baumeister, W., Wildhaber, I. and Engelhardt, H. (1988) Biophys. Chem. 29, 39–49.
[34] Baumeister, W., Wildhaber, I. and Phipps, B.M. (1989) Can. J. Microbiol. 35, 215–227.
[35] Müller, D.J., Schabert, F.A., Büldt, G. and Engel, A. (1995) Biophys. J. 68, 1681–1686.
[36] Saxton, W.O. and Baumeister, W. (1982) J. Microsc. 127, 127–138.
[37] Bretaudiere, J.-P. and Frank, J. (1986) J. Micrsoc. 144, 1–14.
[38] Müller, D.J., Amrein, M. and Engel, A. (1997) J. Struct. Biol. 119, 172–188.